

DISCOVERY OF GEV GAMMA-RAY EMISSION FROM M33 AND ARP 299 WITH *Fermi*–LATSHAO-QIANG XI^{1,2}, RUO-YU LIU^{1,2}, HAI-MING ZHANG^{1,2}, XIANG-YU WANG^{1,2}¹School of Astronomy and Space Science, Nanjing University, Nanjing 210023, China; xywang@nju.edu.cn²Key laboratory of Modern Astronomy and Astrophysics (Nanjing University), Ministry of Education, Nanjing 210023, China

ABSTRACT

Star-forming galaxies are huge reservoirs of cosmic rays (CRs) and these CRs convert a significant fraction of their energy into gamma-rays by colliding with the interstellar medium (ISM). Several nearby star-forming galaxies have been detected in GeV–TeV γ -rays. It is also found that the γ -ray luminosities in 0.1–100 GeV correlate well with indicators of star formation rates of the galaxies, such as the total infrared (IR) luminosity. In this paper, we report a systematic search for possible gamma-ray emission from galaxies in the IRAS Revised Bright Galaxies Sample, using 11.4 years of γ -ray data taken by the *Fermi*–LAT telescope. Two new galaxies, M33 and Arp 299, are detected with significance of $TS \geq 25$. The two galaxies are consistent with the empirical correlation between the γ -ray luminosity and total infrared luminosity, suggesting that their gamma-ray emissions should mainly originate from CRs interacting with ISM. Nevertheless, there is a tentative evidence that the flux of the gamma-ray emission from Arp 299 is variable. If the variability is true, part of the emission should originate from the obscured AGN in this interacting galaxy system. In addition, we find the gamma-ray excess in M33 locates at the northeast region of the galaxy, where a supergiant H II region, NGC 604, resides. This indicates that some bright star-forming regions in spiral galaxies could outshine the bulk of the galaxy disk in producing gamma-ray emission.

1. INTRODUCTION

It is believed that Galactic cosmic rays (CRs) are accelerated by supernova remnant (SNRs) or massive star clusters in our Galaxy. CR protons interact with the interstellar gas and produce neutral pions (schematically written as $p + p \rightarrow \pi^0 + \text{other products}$), which in turn decay into gamma-rays ($\pi^0 \rightarrow \gamma + \gamma$). Seven external star-forming galaxies have been firmly detected in gamma-rays with the Fermi Large Area Telescope (LAT), including the Large Magellanic Cloud (LMC; [Abdo et al. 2010d](#); [Ackermann et al. 2016](#)), the Small Magellanic Cloud ([Abdo et al. 2010b](#)), the Andromeda galaxy M31 ([Abdo et al. 2010c](#)), starburst galaxies M82 and NGC 253 ([Abdo et al. 2010a](#)), NGC 2146 ([Tang et al. 2014](#)) and Arp 220 ([Peng et al. 2016](#); [Griffin et al. 2016](#)). In addition, two star-forming galaxies with obscured AGNs, NGC 1068 and NGC 4945, have been detected by *Fermi*–LAT ([Ackermann et al. 2012](#)).

Noting the connection between star formations and CRs in starburst galaxies, some authors have proposed scaling relationships between star formation rates (SFRs) and gamma-ray luminosities ([Pavlidou & Fields 2002](#); [Torres 2004](#); [Thompson et al. 2007](#); [Stecker 2007](#); [Persic & Rephaeli 2010](#); [Lacki et al. 2011](#)). SFR indicators include the total infrared (IR) luminosity at $8 - 1000 \mu\text{m}$ ([Kennicutt 1998](#)), and radio continuum lu-

minosity at 1.4 GHz produced by synchrotron emitting CR electrons ([Yun et al. 2001](#)). With the accumulation of *Fermi*–LAT data, the correlation between gamma-ray luminosities and SFR indicators are first found in [Abdo et al. \(2010c\)](#). [Ackermann et al. \(2012\)](#) studied a sample of 69 dwarf, spiral, and luminous and ultraluminous IR galaxies using 3 years of data collected by *Fermi*–LAT. They find further evidence for quasi-linear scaling relation between the gamma-ray luminosity and total infrared luminosity which applies both to quiescent galaxies of the Local Group and nearby starburst galaxies. This correlation is later extended to higher luminosity galaxies with gamma-ray detection from a luminous IR galaxy, NGC 2146 ([Tang et al. 2014](#)), and an ultraluminous IR galaxy, Arp 220 ([Peng et al. 2016](#); [Griffin et al. 2016](#)).

In this paper, we report a systematic search for possible gamma-ray emission from galaxies in the IRAS Revised Bright Galaxies Sample, using 11.4 years of γ -ray data taken by the *Fermi*–LAT telescope. While the new detection of GeV emission from M33 and Arp 299 has been briefly mentioned in our previous paper ([Xi et al. 2020](#), hereafter Paper I), here we will present the analysis and relevant discussion in great details. The paper is organized as follows. In §2, we present a description of the galaxy sample selection and the *Fermi*–LAT data analysis procedure. In §3, we present the result of the

analysis. In §4, we discuss the properties of Arp 299 and M33.

2. DATA SET AND ANALYSIS METHODS

The scaling relation reported in [Ackermann et al. \(2012\)](#) implies the gamma-ray detection is likely associated with bright IR galaxies. We selected our sample galaxies from the IRAS Revised Bright Galaxies Sample¹ ([Sanders et al. 2003](#)), excluding the 15 IR-bright galaxies that have been detected in γ -rays with *Fermi*-LAT and listed in *Fermi*-LAT Fourth Source Catalog (4FGL; [The Fermi-LAT collaboration 2019](#)). We performed the standard sequence of analysis steps for each galaxies (described in our Paper I), resulting in the detection of two new γ -ray sources that are, respectively, spatially coincident with M33 and Arp 299. The details of the analysis for these two galaxies are given as below.

Fermi-LAT is a pair-conversion telescope covering the energy range from 20 MeV to more than 300 GeV with a field of view of 2.4 sr ([Atwood et al. 2009](#)). For the analysis in this work, we employed recent developments of the Science Tools and use the *Fermi*-LATsource class events collected in ~ 11.4 years, which include both the front and back section of the LAT, but exclude the events with a zenith angle larger than 90° in order to remove the contaminant from the Earth limb.

For the galaxy M33, we selected the events in the energy range $0.3 - 500$ GeV and within a rectangular region-of-interest (ROI) of size $17^\circ \times 17^\circ$ centered at M33 IR center ($\alpha_{2000} = 23.475^\circ, \delta_{2000} = 30.669^\circ$). We used *gtmktime* tool to select time intervals expressed by (DATA_QUAL > 0) && (LAT_CONFIG == 1), and binned the data in 20 logarithmically spaced bins in energy and in a spatial bin of 0.025° per pixel². The gamma-ray background model consists of the latest template *gll_iem_v7.fits* for Galactic interstellar emission and the isotropic template with the spectrum *iso_P8R3_SOURCE_V2_v01.txt*, as well as the sources listed in the 4FGL catalog within 20° around M33. One possible shortcoming of using the 4FGL catalog (based on 8 years of LAT observations) to perform the search within a data set covering 11.4 yr is that unrelated new point sources may be discovered inside the ROI of the target source, which may influence the analysis. We pro-

duce a $6^\circ \times 6^\circ$ map of the Test Statistic (TS)³ centered at M33 to search new background γ -ray sources. The criteria of the new source is that the γ -ray excess has a significance of $TS > 25$ above the diffuse background and has an angular separation larger than 0.3° from the center of M33. We find three new background sources and include them in our background model for M33 (see the appendix A).

For the galaxy Arp 299, we selected the events in the energy range $0.3 - 500$ GeV within a rectangular ROI of size $17^\circ \times 17^\circ$ centered at the galaxy IR center ($\alpha_{2000} = 172.136^\circ, \delta_{2000} = 58.561^\circ$). The rest steps, i.e., the data filter, data bin and background modeling are carried out with similar approaches to what have been done for M33. There is a new background source in the $6^\circ \times 6^\circ$ region centered at Arp 299.

In the likelihood analysis, we set each source within 6.5° from the ROI center a free normalization (the 68% containment radius of photons at normal incidence with an energy of 300 MeV is roughly 2.5°). This choice ensures that 99.9% of the predicted γ -ray counts is contained within the chosen radius. The normalizations of the Galactic and isotropic diffuse components are always left free.

3. DATA ANALYSIS RESULTS

3.1. M33

3.1.1. Morphological analysis

[Fig.1](#) shows the $0.6^\circ \times 0.6^\circ$ TS map in $0.3 - 500$ GeV around M33. We find that the position of the TS peak locates at the northeast part of the galaxy. We first explored the point source models at the best-fit location (i.e., the position of the peak TS value) and at the center of M33 respectively. The TS values are respectively 25.1 and 16.7, which suggests that source is likely to be offset from the galaxy center. In addition, we considered spatially extended templates based on Herschel/PACS map at $160 \mu\text{m}$ and IRAS map at $60 \mu\text{m}$. These templates are used to test the spatial correlation of the gamma-ray emission with star formation sites. The Herschel/PACS and IRAS map models provide a better fit to the data than the point source model at the center of M33, but gives an almost equally good fit as the point source model at the best location. We also test the uniform-brightness disk model centered at the optical center of M33, for which the size is optimized to be 0.23° . We do not find any improvement over the point source model at the best-fit location. The results

¹ This is a complete flux-limited sample of all extragalactic objects brighter than 5.24 Jy at $60 \mu\text{m}$, covering the entire sky surveyed by IRAS at Galactic latitudes $|b| > 5^\circ$.

² For a new detection of gamma-ray point source, the best location and uncertainty are determined by maximizing the likelihood value and using the distribution of Localization Test Statistic (LTS), defined by twice the logarithm of the likelihood ratio of any position with respect to the maximum. We find that the location derived by binned likelihood analysis using the spatial bin 0.025° is consistent with that given by Fermi tool *gtfindsrc* used in unbinned likelihood analysis.

³ TS is defined as $TS = -2(\ln L_0 - \ln L)$, where L_0 is the maximum-likelihood value for null hypothesis and L is the maximum-likelihood with the additional point source with a power-law spectrum.

Table 1.

Spatial model	TS	<i>R.A.</i> [deg]	(Decl.) [deg]	$F_{0.1-100\text{GeV}}$ [$10^{-12} \text{ erg cm}^{-2} \text{ s}^{-1}$]	Γ	N_{dof}
M33						
Point source (at TS_{peak})	25.1	23.609	30.784	1.28 ± 0.42	2.23 ± 0.24	4
Point source (at center)	16.7	23.475	30.669	1.34 ± 0.47	2.41 ± 0.26	2
0.23° Disk (at center)	23.2	23.475	30.669	1.55 ± 0.35	2.22 ± 0.42	3
Herschel/PACS (160 μm)	22.8			1.48 ± 0.40	2.22 ± 0.42	2
IRAS (60 μm)	23.9			1.52 ± 0.40	2.20 ± 0.43	2
Arp 299						
Point source (at TS_{peak})	27.8	172.050	58.526	1.08 ± 0.28	2.07 ± 0.20	4
Point source (at center)	26.4	172.136	58.561	1.08 ± 0.29	2.12 ± 0.21	2

NOTE—The spectrum of each spatial model is modeled as a power law spectrum $dN/dE = N_0(E/E_0)^{-\Gamma}$, where E_0 is fixed to 3 GeV.

of all considered morphological tests are shown in Table 1.

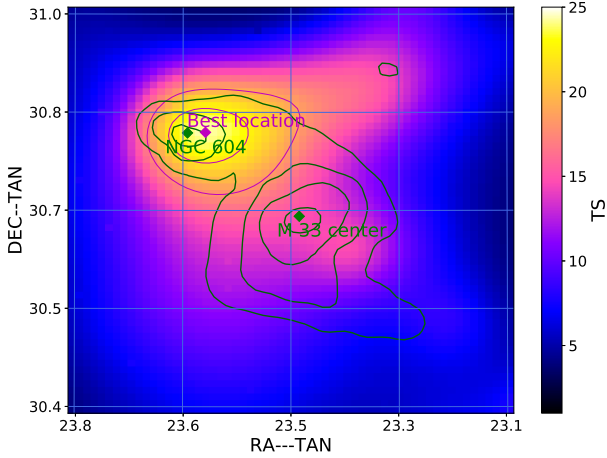


Figure 1. TS map in the energy band 0.3 – 500 GeV around M33. The purple contours correspond to 68% and 95% confidence region assuming the point-like source template. The dark green contours correspond to the map of IR flux measured by IRAS at 60 μm .

3.1.2. Flux variability

We retained the point source model at the best location for examining the variability of the gamma-ray flux. We computed a light curve in 4 and 8 time bins over 11.4 years, for events in the energy range 0.3 – 500 GeV. In each time bin, all sources within 6.5° region around M33 have spectra fixed to the shapes obtained from the above broad band analysis. The results is shown in Figure 2. We then used a likelihood-based statistic to test

the significance of the variability. Following the definition in 2FGL (Nolan et al. 2012), the variability index from the likelihood analysis is constructed, with a value in the null hypothesis where the source flux is constant across the full time period, and the value under the alternate hypothesis where the flux in each bin is optimized: $TS_{\text{var}} = \sum_{i=1}^N 2 \times (\text{Log}(L_i(F_i)) - \text{Log}(L_i(F_{\text{mean}})))$, where L_i is the likelihood corresponding to bin i , F_i is the best-fit flux for bin i , and F_{mean} is the best-fit flux for the full time assuming a constant flux. We get $TS_{\text{var}} = 1.3 - 1.6\sigma$ for different time bins, which suggests no significant variability for M33.

3.1.3. Spectral Analysis

For the spectral analysis of M33, we performed a binned maximum likelihood fitting in the 0.3 – 500 GeV energy range with 20 logarithmic energy bins in total. The power law indices are consistent with each other for the four spatial models, as shown in table 1. We also generated the spectral points based on a maximum likelihood analysis with 5 logarithmic energy bins over 0.1 – 500 GeV. Within each bin, we used the point source model at the best location and the power law spectrum with a fixed index of $\Gamma = 2$ and a free normalization. For the background diffuse components and sources within 6.5° of M33, we fixed their spectral indices to the best-fit values obtained from the above background fitting, but allowing the normalization to vary. We find the best-fit power-law model is consistent with the spectral points, as shown in Fig 3.

3.2. Arp 299

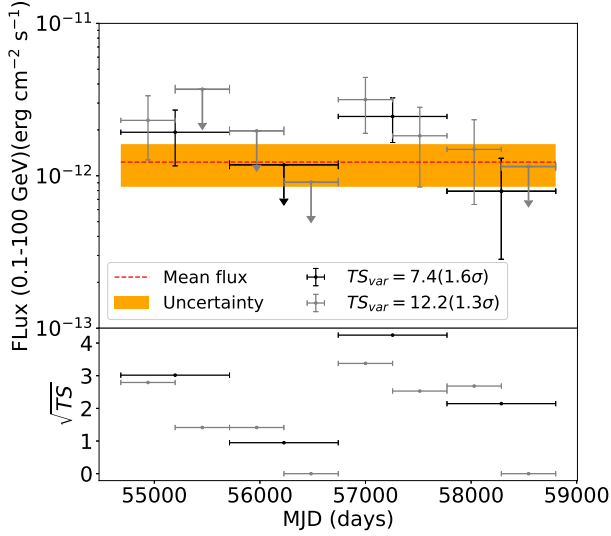


Figure 2. Light curves of M33 with 4 and 8 time bins. The mean flux are given by using the ~ 11.4 year analysis. The upper limits at 95% confidence level are derived when the TS value for the data points are lower than 4.

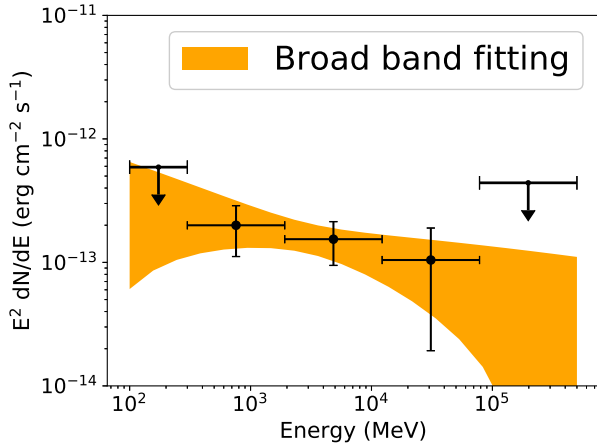


Figure 3. SED for M33. The yellow band denotes the power-law fitting of the spectral data in energy band 0.3–500 GeV. The upper limits at 95% confidence level are derived when the TS value for the data point is lower than 4 ($< 2\sigma$).

3.2.1. Morphological analysis

Fig. 4 shows the $0.5^\circ \times 1^\circ$ TS map in the 0.3–500 GeV energy range around the galaxy Arp 299. We find that the galaxy position is located within the 68% confidence region of the gamma-ray sources. We also explored the point source models located at the peak TS position and at the center of Arp 299, respectively, obtaining comparable TS values (See Table. 1).

3.2.2. Flux variability

To examine the variability of the gamma-ray flux from Arp 299, we computed light curves in 4 and 8 time bins over 11.4 years for events in the energy range 0.3–500 GeV. We followed a procedure similar to that

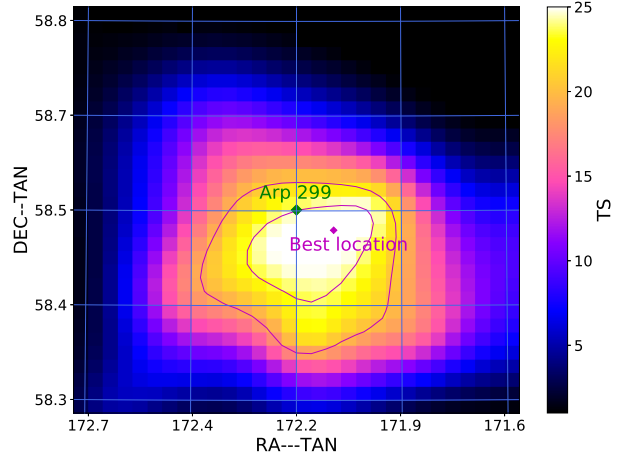


Figure 4. TS map in the energy band 0.3–500 GeV for Arp 299. The purple contours correspond to 68% and 95% confidence region assuming the point-like source template. The dark green contours correspond to the map of IR flux measured by IRAS at $60\mu\text{m}$.

used for M33 in Section 3.1.2, and the result is shown in Figure 5. We obtain a variability significance of $2.6 - 2.9\sigma$ for different time bins, which suggests a mildly significant variability in the gamma-ray emission of Arp 299.

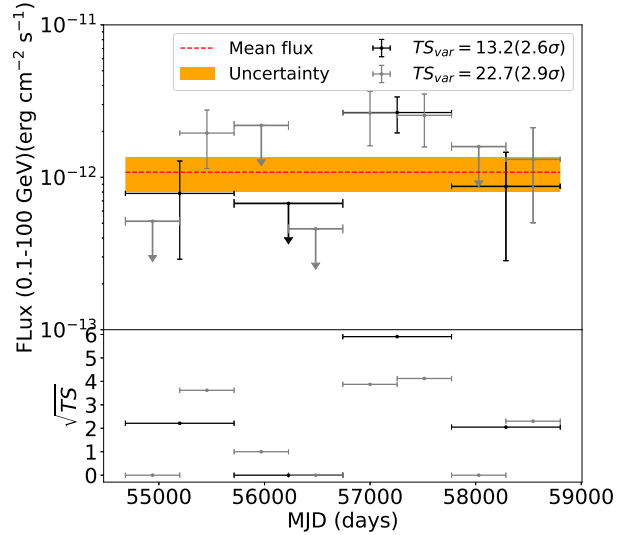


Figure 5. Light curve and TS with 4 and 8 time bins for Arp 299. The mean flux are given by using the ~ 11.4 year analysis. The upper limits at 95% confidence level are derived when the TS value for the data points are lower than 4.

3.2.3. Spectral Analysis

For the spectral analysis of Arp 299, we performed a binned maximum likelihood fitting in the 0.3–500 GeV energy range with 20 logarithmic energy bins in total, considering two spatial models. The result is shown in Table. 1. We also generated the spectral points deter-

mined by performing a maximum likelihood analysis in 5 logarithmically space energy bins over $0.1 - 500$ GeV similar to the case of M33 in Section 3.1.3. As shown in Figure 6, the best-fit power-law model is consistent with spectral points.

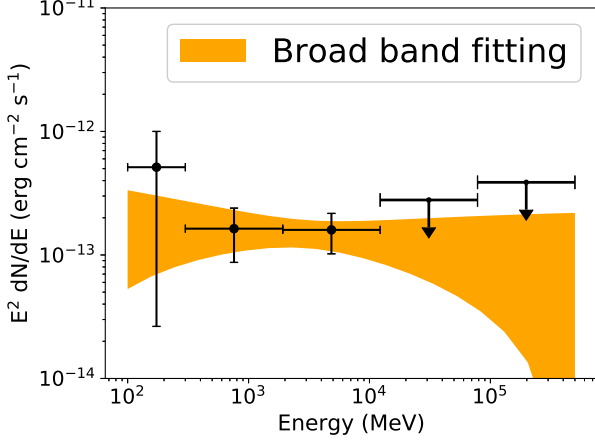


Figure 6. SED for Arp 299. The yellow band represent the power-law fitting of the spectral data in energy band $0.3 - 500$ GeV. The upper limits at 95% confidence level are derived when the TS value for the data points are lower than 4.

3.3. Non-detected IR galaxies

We derived the 95% C.L. upper limits (UL) for each non-detected galaxy (i.e., $TS < 25$) using the Bayesian method assuming a power-law spectra shape with a fixed photon index of -2.2 . For NGC 2403, we attribute the gamma-ray emission, which appears only in the first 5.7-year *Fermi*-LAT observation, to SN 2004dj (see Paper I). Using the second 5.7-year *Fermi*-LAT data, we derived an upper limit for NGC 2403 assuming a point source model at the galaxy’s center. We compare the ULs on the gamma-ray luminosity ($0.1 - 100$ GeV) to the total IR luminosity ($8 - 1000 \mu\text{m}$) for these non-detected IR galaxies, which is shown in Fig 7. We find these non-detected IR galaxies are basically consistent with the $L_\gamma - L_{\text{IR}}$ correlation.

4. DISCUSSIONS AND CONCLUSIONS

4.1. M33

As the third largest galaxy in our Local Group, M33 has been considered to be a promising gamma-ray source due to its proximity and relatively high gas masses and star formation activity. By using nearly 2 years of *Fermi*-LAT data, Abdo et al. (2010c) searched for the γ -ray emission from M33, but no significant gamma-ray emission was detected. Ackermann et al. (2017) revisited the gamma-ray emission in the direction M33 using more than 7 yr of LAT Pass 8 data in the energy

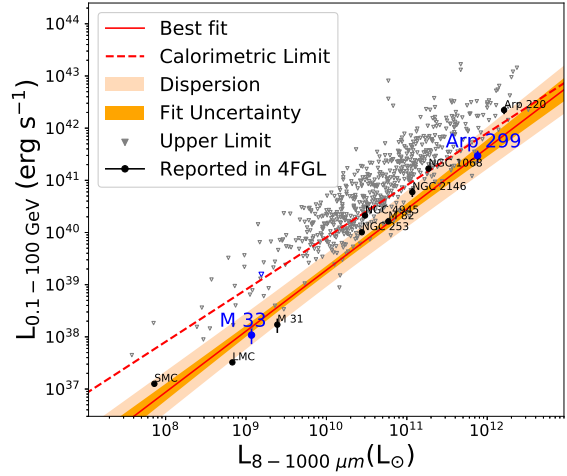


Figure 7. Gamma-ray luminosity ($0.1 - 100$ GeV) v.s. total IR luminosity ($8 - 1000 \mu\text{m}$) for nearby star-forming galaxies. The yellow band represents the empirical correlation $\log(L_{0.1-100 \text{ GeV}}/\text{erg s}^{-1}) = (1.17 \pm 0.07)\log(L_{8-1000 \mu\text{m}}/10^{10} L_\odot) + (39.28 \pm 0.08)$ with an intrinsic dispersion normally distributed in the logarithmic space with a standard deviation of $\sigma_D = 0.24$ (Ackermann et al. 2012). The gamma-ray luminosities for the galaxies reported in 4FGL are derived from the catalog value (The *Fermi*-LAT collaboration 2019). The IR luminosities are from Sanders et al. (2003). The blue upper downward triangle represents the upper limit for NGC 2403.

range $0.1 - 100$ GeV, but still found no significant detection. More recently, Karwin et al. (2019) and Di Mauro et al. (2019) found positive residual towards the M33 region, but their analyses do not consider new background sources around M33 (see the Appendix). We find that these new background sources affect the morphology and the significance of the signal.

Our measurement gives a flux of $(1.28 \pm 0.42) \times 10^{-12} \text{ erg cm}^{-2} \text{ s}^{-1}$ in the energy range $0.1 - 100$ GeV, implying a luminosity of $\sim 1.1 \times 10^{38} \text{ erg s}^{-1}$. In Figure 7, we show the position of M33 on the well-known correlation between the γ -ray luminosity in $0.1 - 100$ GeV and the total IR luminosity ($8 - 1000 \mu\text{m}$) for local group galaxies and nearby star forming galaxies (Ackermann et al. 2012; Peng et al. 2016). M33 agrees well with this correlation, indicating that the gamma-ray emission of M33 may arise from the CR-ISM interaction process.

The TS map of M33 shows that the gamma-ray emission locates at the northeast region of the galaxy, where a supergiant H II region NGC 604 resides. NGC 604 is the second most massive H II region in the Local Group and it has a relatively high star-formation rate. From the H I density distribution map of M33, an over-density of H I gas filament is seen around that region, with a column density about $30 M_\odot \text{ pc}^{-2}$ (Engargiola et al. 2003). Such a high-density region provides a thick target for pp collisions, so the efficiency for the pp collision is expected

to be high.

The energy-loss time of protons due to the pp collision t_{loss} can be expressed as $(0.5n\sigma_{pp}c)^{-1}$, where 0.5 is the inelasticity, n is the hydrogen atom number density and σ_{pp} is the inelastic pp collision cross section. Converting the atom number density to gas surface density, $\Sigma_g = m_p n H$, where m_p is the mass of proton and H is the size of the over-density region, the energy-loss time is

$$t_{\text{loss}} = 6.5 \times 10^6 \left(\frac{H}{200 \text{ pc}} \right) \left(\frac{\sigma_{pp}}{30 \text{ mb}} \right)^{-1} \left(\frac{\Sigma_g}{30 M_\odot \text{ pc}^{-2}} \right)^{-1} \text{ yr} \quad (1)$$

where H is the typical width of an H I filament.

CRs are scattered off small-scale magnetic field inhomogeneities randomly and diffuse out of the H I filament. The diffusive escape time is $t_{\text{diff}} = H^2/4D$. Here $D = D_0 (E/E_0)^\delta$ is the diffusion coefficient, where D_0 and $E_0 = 3 \text{ GeV}$ are normalization factors, and $\delta = 0 - 1$ depending on the spectrum of interstellar magnetic turbulence. The diffusion time is

$$t_{\text{diff}} = 3 \times 10^5 \left(\frac{H}{200 \text{ pc}} \right)^2 \left(\frac{D_0}{10^{28} \text{ cm}^2 \text{ s}^{-1}} \right)^{-1} \left(\frac{E_p}{3 \text{ GeV}} \right)^{-\delta} \text{ yr}. \quad (2)$$

With $D_0 \sim 10^{27} \text{ cm}^2 \text{ s}^{-1}$, the escape time is comparable to the pp cooling time, and the region may be considered to be a proton calorimeter. Although this value is one order of magnitude smaller than the standard diffusion coefficient in the ISM of our Galaxy, it is not *a priori* impossible. A recent polarisation analysis on Cygnus-X, a massive star-forming region in our Galaxy, has revealed that the turbulence in the region is dominated by the magnetosonic mode (Zhang et al. 2018), which is more effective than the commonly considered Alfvénic mode in CR confinement (Yan & Lazarian 2002). There are also a few giant molecular clouds with mass up to $10^6 M_\odot$ spatially associated with NGC 604 (Engargiola et al. 2003), which would enhance the average atom density and subsequently the gamma-ray emissivity by a factor of a few in that region. In addition, massive stellar winds are probably efficient CR factories (Casse & Paul 1980; Cesarsky & Montmerle 1983; Aharonian et al. 2019), so we expect the CR flux around NGC 604 to be higher than the average CR flux in the ISM. These may explain why the peak of γ -ray emission locates in the northeast region of M33.

4.2. Arp 299

Arp 299 is one of the most powerful star-forming galaxies in the local Universe, at a distance of 44 Mpc (Heckman et al. 1999). With a total IR luminosity of $L_{\text{IR}} = 5.16 \times 10^{11} L_\odot$ (Charmandaris et al. 2002), it belongs to the class of Luminous IR Galaxies (LIRGs). The system consists of two galaxies in an advanced merging state, NGC 3690 to the west and IC 694 to the

east, plus a small compact galaxy to the northwest (Hibbard & Yun 1999). BeppoSAX revealed for the first time the existence of a deeply buried ($N_H = 2.5 \times 10^{24} \text{ cm}^2$) AGN with a unabsorbed luminosity of $L_{0.5-100 \text{ keV}} = 1.9 \times 10^{43} \text{ erg s}^{-1}$ (Della Ceca et al. 2002). Chandra and XMM-Newton observations later confirmed the existence of a strongly absorbed AGN and located it in the nucleus of NGC 3690, while there is evidence that the second nucleus IC 694 might also host an AGN of lower luminosity (Zezas et al. 2003; Ballo et al. 2004; Iwasawa et al. 2009; Pérez-Torres et al. 2010; Della Ceca et al. 2002; Alonso-Herrero et al. 2013). According to the correlation between the X-ray luminosity ($L_{2-10 \text{ keV}}$) and the bolometric luminosity (L_{bol}) of X-ray selected AGN (Rosario et al. 2012), we find an intrinsic luminosity of $L_{\text{bol}} \simeq 5 \times 10^{43} \text{ erg s}^{-1}$ for the obscured AGN. Even if all the AGN luminosity is reprocessed into the IR band, its contribution is negligible to the measured IR luminosity from the galaxy and hence the latter is related to the star-forming process in Arp 299, as in other star-forming galaxies.

As shown in 5, there is a tentative evidence of flux variability in Arp 299. If this variability is true, it may be due to the contribution from the obscured AGN. Some other merging galaxy systems, such as NGC 3424, also show flux variability in gamma-ray emission (Peng et al. 2019). However, different from NGC 3424, Arp 299 lies on the correlation line between the γ -ray luminosity and total IR luminosity for star-forming galaxies (see Fig.1). This may indicate that a subdominant contribution to gamma-ray flux from the obscured AGN.

4.3. Summary

To summarize, our analysis using 11.4 years of *Fermi*-LAT observations results in new detections of gamma-ray emission from M33 and Arp 299. The fluxes of both sources are consistent with the correlation between the gamma-ray luminosity and the total IR luminosity for star-forming galaxies, suggesting that the gamma-ray emissions from the sources arise mainly from CRs interacting with the ISM in the galaxies. However, it is found that there is a tentative evidence of variability in the gamma-ray flux of Arp 299. The variability can be tested in future with longer observation time. If the variability is true, at least part of the gamma-ray emission should come from the obscured AGN in Arp 299. The morphological analysis of the gamma-ray emission from M33 shows that the peak of the TS map is not located at the galaxy center, but coincident with a supergiant H II region NGC 604. This implies that some bright star-forming regions could dominate over the bulk of the galaxy disk in producing the gamma-ray emission.

A note added: We note that during the final stage of the present work, an independent research paper (Ajello

et al. 2020) appears online conducting a similar study to that of the present work.

REFERENCES

- Abdo, A. A., Ackermann, M., Ajello, M., et al. 2010a, *ApJL*, 709, L152
- . 2010b, *A&A*, 523, A46
- . 2010c, *A&A*, 523, L2
- . 2010d, *A&A*, 512, A7
- Acero, F., Ackermann, M., Ajello, M., et al. 2016, *ApJS*, 223, 26
- Ackermann, M., Ajello, M., Allafort, A., et al. 2012, *ApJ*, 755, 164
- Ackermann, M., Albert, A., Atwood, W. B., et al. 2016, *A&A*, 586, A71
- Ackermann, M., Ajello, M., Albert, A., et al. 2017, *ApJ*, 836, 208
- Aharonian, F., Yang, R., & de Oña Wilhelmi, E. 2019, *Nature Astronomy*, 3, 561
- Alonso-Herrero, A., Roche, P. F., Esquej, P., et al. 2013, *ApJL*, 779, L14
- Atwood, W. B., Abdo, A. A., Ackermann, M., et al. 2009, *ApJ*, 697, 1071
- Ajello, M., Di Mauro, M., Paliya, V. S. and Garrappa, S., 2020, *arXiv:2003.05493*
- Ballo, L., Braito, V., Della Ceca, R., et al. 2004, *ApJ*, 600, 634
- Casse, M., & Paul, J. A. 1980, *ApJ*, 237, 236
- Cesarsky, C. J., & Montmerle, T. 1983, *SSRv*, 36, 173
- Charmandaris, V., Stacey, G. J., & Gull, G. 2002, *ApJ*, 571, 282
- Della Ceca, R., Ballo, L., Tavecchio, F., et al. 2002, *ApJL*, 581, L9
- Di Mauro, M., Hou, X., Eckner, C., Zaharijas, G., & Charles, E. 2019, *PhRvD*, 99, 123027
- Engargiola, G., Plambeck, R. L., Rosolowsky, E., et al. 2003, *ApJS*, 149, 343
- Griffin, R. D., Dai, X., & Thompson, T. A. 2016, *ApJL*, 823, L17
- Heckman, T. M., Armus, L., Weaver, K. A., & Wang, J. 1999, *ApJ*, 517, 130
- Hibbard, J. E., & Yun, M. S. 1999, *AJ*, 118, 162
- Iwasawa, K., Sanders, D. B., Evans, A. S., et al. 2009, *ApJL*, 695, L103
- Karwin, C. M., Murgia, S., Campbell, S., & Moskalenko, I. V. 2019, *ApJ*, 880, 95
- Kennicutt, Robert C., J. 1998, *ApJ*, 498, 541
- Lacki, B. C., Thompson, T. A., Quataert, E., Loeb, A., & Waxman, E. 2011, *ApJ*, 734, 107
- Nolan, P. L., Abdo, A. A., Ackermann, M., et al. 2012, *ApJS*, 199, 31
- Pavlidou, V., & Fields, B. D. 2002, *ApJL*, 575, L5
- Peng, F.-K., Wang, X.-Y., Liu, R.-Y., Tang, Q.-W., & Wang, J.-F. 2016, *ApJL*, 821, L20
- Peng, F.-K., Zhang, H.-M., Wang, X.-Y., Wang, J.-F., & Zhi, Q.-J. 2019, *ApJ*, 884, 91
- Pérez-Torres, M. A., Alberdi, A., Romero-Cañizales, C., & Bondi, M. 2010, *A&A*, 519, L5
- Persic, M., & Rephaeli, Y. 2010, *MNRAS*, 403, 1569
- Rosario, D. J., Santini, P., Lutz, D., et al. 2012, *A&A*, 545, A45
- Sanders, D. B., Mazzeella, J. M., Kim, D. C., Surace, J. A., & Soifer, B. T. 2003, *AJ*, 126, 1607
- Stecker, F. W. 2007, *Astroparticle Physics*, 26, 398
- Tang, Q.-W., Wang, X.-Y., & Tam, P.-H. T. 2014, *ApJ*, 794, 26
- The Fermi-LAT collaboration. 2019, *arXiv e-prints*, *arXiv:1902.10045*
- Thompson, T. A., Quataert, E., & Waxman, E. 2007, *ApJ*, 654, 219
- Torres, D. F. 2004, *ApJ*, 617, 966
- Xi, S. Q., Liu, R. Y., Wang, X. Y., Yang, R. Z., Yuan, Q., Zhang, B., 2020, *arXiv:2003.04795* (Paper I)
- Yan, H., & Lazarian, A. 2002, *PhRvL*, 89, 281102
- Yun, M. S., Reddy, N. A., & Condon, J. J. 2001, *ApJ*, 554, 803
- Zezas, A., Ward, M. J., & Murray, S. S. 2003, *ApJL*, 594, L31
- Zhang, H., Chepurinov, A., Yan, H., et al. 2018, *arXiv e-prints*, *arXiv:1808.01913*

APPENDIX

A. BACKGROUND MODEL FOR M 33 AND ARP 299

As shown in Fig A1, we generated the $6^\circ \times 6^\circ$ TS map based on the background modeling by the combination of diffuse model components and the sources listed in 4FGL catalog. For the region around M 33 and Arp 299, we found three and one obvious excesses outside the galaxy radii, respectively. We locate these four new point sources at the positions of the TS peak and derived their power-law spectral parameter from a broadband spectral fit. The coordinates of four new point sources and their spectral parameters are given in Table A1.

To study the impact of the diffuse Galactic emission models, we also created an alternative background model using the old diffuse Galactic emission template (i.e., *glliem_v06.fits* and isotropic model shaped by *iso_P8R3_SOURCE_V2_v01.txt* (Acero et al. 2016)). We generated the TS map for M 33 and for Arp 299 based on this background model. Comparing the new map (see Fig A2) to that shown in Fig.1 and Fig.4, we find that the impact of different diffuse Galactic emission models is not important.

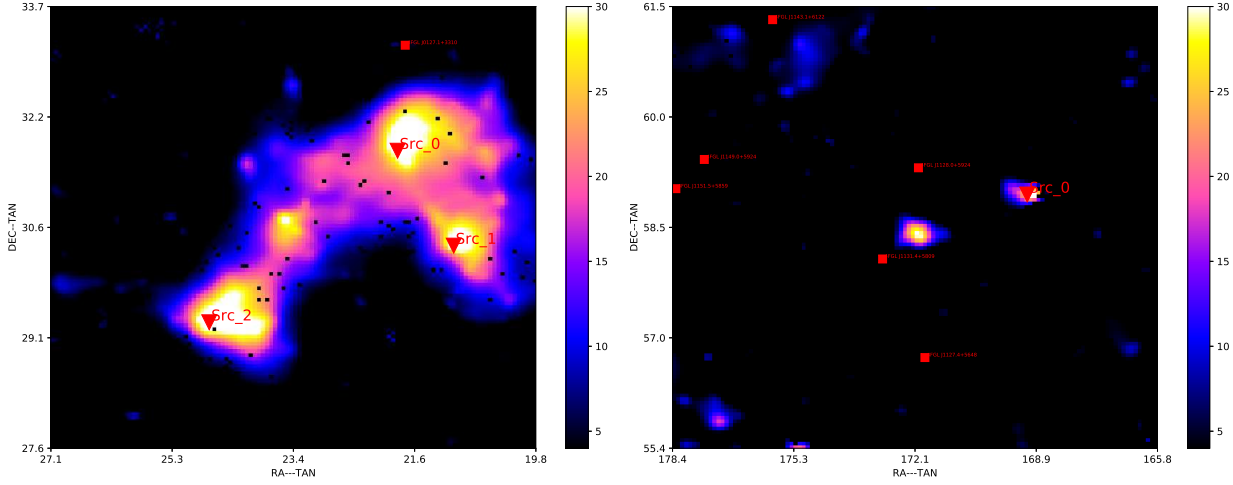


Figure A1. $6^\circ \times 6^\circ$ TS map in the energy band $0.3 - 500$ GeV for M 33 (left) and for Arp 299 (right) for surveying the new background sources. The dark green contours correspond to measurements of IRAS at $60\mu\text{m}$.

Table A1.

Name	TS	$R.A.$ [deg]	(Decl.) [deg]	N_0 $\times 10^{-13}$	Γ
$6^\circ \times 6^\circ$ region around M33					
Src_0	34.1	21.918	31.734	2.07 ± 0.43	2.72 ± 0.23
Src_1	29.3	21.127	30.423	2.05 ± 0.43	2.74 ± 0.22
Src_2	38.5	24.651	29.389	2.41 ± 0.43	2.87 ± 0.20
$6^\circ \times 6^\circ$ region around Arp 299					
Src_0	32.7	169.369	59.006	0.47 ± 0.02	1.73 ± 0.17

NOTE—The spectrum of each sources is modeled as a power law spectrum $dN/dE = N_0(E/E_0)^{-\Gamma}$, where E_0 is fixed to 1 GeV.

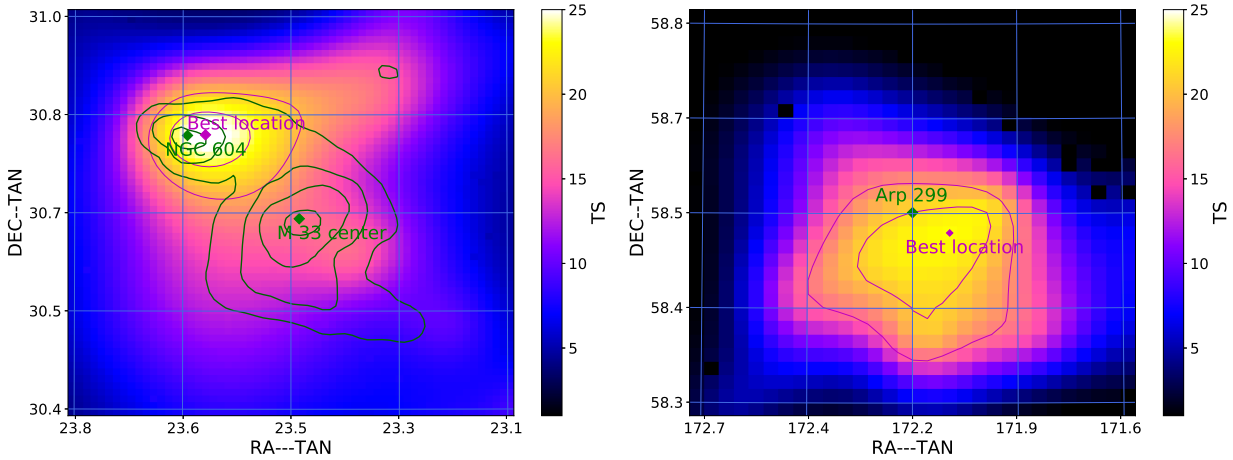


Figure A2. TS map in the energy band $0.3 - 500$ GeV for M33 (left) and for Arp 299 (right) with background emission subtracted for the case using the old diffuse Galactic emission template `gll_iem_v06.fits`.